JGR Oceans

RESEARCH ARTICLE
10.1029/2020JC016713

Slope-Intensified Storm-Induced Near-Inertial Oscillations in the South China Sea

Ruixiang Li[1,2,3], Changsheng Chen[4], Wenjie Dong[5], Robert C. Beardsley[6], Zhongxiang Wu[4], Wenping Gong[7], Yuqiang Liu[2,3], Tongmu Liu[2,3], and Danya Xu[8]

[1]South China Sea Resource Exploitation and Protection Collaborative Innovation Center, School of Marine Sciences, Sun Yat-sen University, Guangzhou, China, [2]South China Sea Marine Survey and Technology Center, State Ocean Administration, Guangzhou, China, [3]Key Laboratory of Marine Environmental Survey Technology and Application, Ministry of Natural Resources, Guangzhou, China, [4]School for Marine Science and Technology, University of Massachusetts-Dartmouth, New Bedford, MA, USA, [5]School of Atmospheric Sciences, Sun Yat-sen University, Guangzhou, China, [6]Department of Physical Oceanography, Woods Hole Oceanographic Institution, Woods Hole, MA, USA, [7]School of Marine Sciences, Sun Yat-sen University, Guangzhou, China, [8]Southern Marine Science and Engineering Guangdong Laboratory, Zhuhai, China

Key Points:

- Tropical storm-generated near-inertial oscillations exhibited a slope-intensified feature no matter what its trajectories were
- Oscillations had two maximum amplitudes in the upper mixed and stratified layers, with a phase changing rapidly through thermoclines
- Strongest near-inertial oscillations occurred during an adjustment period of low-frequency flow to the pre-storm state

Correspondence to:
R. Li and C. Chen,
liruix6@mail2.sysu.edu.cn;
c1chen@umassd.edu

Citation:
Li, R., Chen, C., Dong, W., Beardsley, R. C., Wu, Z., Gong, W., et al. (2021). Slope-intensified storm-induced near-inertial oscillations in the South China Sea. *Journal of Geophysical Research: Oceans*, *126*, e2020JC016713. https://doi.org/10.1029/2020JC016713

Received 13 AUG 2020
Accepted 9 FEB 2021

Abstract The South China Sea (SCS) is a region vulnerable to tropical cyclones (TCs). An array of moored current meters and meteorological buoys was deployed within major pathways of TCs across the slope of the northern shelf of the SCS from September 1, 2017 through September 30, 2018. Three TCs, Khanun, SonTinh, and Mangkhut, traversed by the storm-monitoring array in October 2017, July, and September 2018, respectively. Storm-generated near-inertial oscillations (NIOs) were observed at the moorings. These oscillations exhibited a slope-intensified feature regardless of the trajectories and intensities of TCs. In the stratified area, the NIOs was characterized by a two-layer structure, with large amplitudes in the mixed layer and beneath thermoclines. The phases of these oscillations changed rapidly through thermoclines. No significant nonlinear interactions were found between near-inertial and tidal currents. The low-frequency flow over the slope was characterized by a southwestward current in the along-shelf direction and an onshore current above the bottom boundary, and a weak offshore current near the bottom in the cross-shelf direction. The flow-induced negative vorticity was intensified during the TCs and appearances of mesoscale eddies. Slope-intensified NIOs can be explained by topographic inertial waves and energy trapping due to the negative vorticity of the slope flow. The strongest NIOs always occur during an adjustment period of the low-frequency flow to a pre-storm condition, suggesting a significant energy transfer from the low-frequency flow to the inertial motion.

Plain Language Summary Near-inertial oscillations (NIOs) are a common feature caused by restoring force due to Earth's rotation. In the South China Sea (SCS), NIOs are often observed over the continental shelf during tropical cyclone (TC) events as oceanic responses to the sudden change of the storm's wind direction. Due to a lack of simultaneous observations, no efforts have been made to examine the cross-shelf variation of storm-induced NIOs over the slope of the SCS. An array with eight moored current meters and two meteorological buoys was deployed over the northern SCS shelf from September 1, 2017 through September 30, 2018. Three TCs, Khanun, SonTinh, and Mangkhut, traversed by the storm-monitoring array in October 2017, July, and September 2018, respectively. Regardless of the trajectories and intensities of TCs, the storm-generated NIOs exhibited a slope-intensified feature. The SCS slope is characterized by the persistent density front and along-shelf subtidal flow. The flow-induced negative vorticity was intensified during the storms. The slope-intensified NIOs are likely associated with topographically trapped inertial waves and energy-trapping by the flow-induced negative vorticity. The strongest NIOs occur during the restoring period of subtidal flow to the pre-storm condition, suggesting an energy transfer from the low-frequency flow to the inertial motion.

1. Introduction

Near-inertial oscillations (NIOs) are commonly observed in the ocean as responses to a sudden change of the wind direction during passages of either cold fronts or tropical cyclones (TCs, D'Asaro, 1985; Pollard, 1970; Shay & Elsberry, 1987; Shay et al., 1989). The wind-induced NIOs can form in both homogeneous

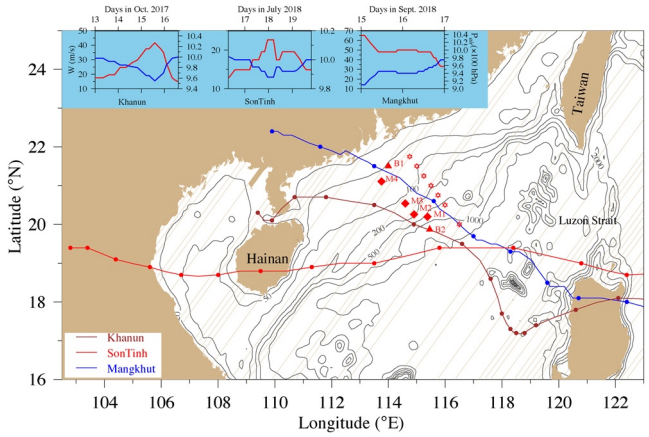

Figure 1. Locations of moorings, buoys, and hydrographic survey sites overlapping by trajectories of Typhoons Khanun, Tropical Storm SonTinh, and Typhoon Mangkhut. Filled circles on trajectories indicate the locations of the typhoon's center over a 6 h interval starting at 2:00 CST, October 13, 2017, for Khanun, 20:00 CST, July 16, 2018, for SonTinh, and 2:00 CST, September 15, 2018, for Mangkhut, respectively. Red filled diamonds indicate the locations of moorings M1, M2, M3, and M4. Red filled triangles indicate the locations of meteorological buoys. Hexagrams are the hydrographic survey sites taken on November 17, 2017, and September 23, 2018. The upper-left panels represent the time series of the maximum wind (red curve) and central pressure (blue curve) of Khanun (left), SonTinh (middle), and Mangkhut (right).

and stratified conditions. Under a stratified condition, the NIOs excited in the mixed layer can transfer the energy through the thermocline to produce near-inertial internal waves in the deep region (Chen et al. 1996; Qi et al., 1995; Shay & Elsberry, 1987). Previous observations reveal that storm-generated near-inertial currents can reach ~150 cm/s near the surface (Sanford et al., 2011), with a spatial scale of 10 ~ 100 km (Alford et al., 2016). Since the energy flux of wind-generated NIOs is the same order of magnitude as the baroclinic tidal motion, it has been considered as an important contributor to global energy balance (Alford, 2001a).

The South China Sea (SCS) is the largest marginal sea in the Western Pacific Ocean, which is frequently influenced by TCs (Wang et al., 2007). The NIOs are often triggered by either TCs or the onset of the Asian monsoon (Cao et al., 2018; Sun et al., 2015; Shu et al., 2016; Sun, Hu, et al., 2011; Sun, Zheng, et al., 2011). The observed magnitudes of NIOs vary in the range of 10–60 cm/s with a duration of >3–10 days (Chen et al., 2013; 2015; Guan et al., 2014; Sun et al., 2012; Yang et al., 2015). The near-inertial kinetic energy also exhibits a seasonal variability with a maximum in August through October (Chen et al., 2013). In a stratified region, the NIOs are dominated by the first baroclinic mode in the vertical, with opposite phases in the upper mixed and lower stratified layers (Chen, et al., 2015; Yang et al., 2015). The vertical structure of NIOs in the SCS is similar to the NIOs observed over the New England shelf (Mackinnon & Gregg, 2005; Shearman, 2005;) and Louisiana-Texas (LATEX) shelf (Chen et al., 1996). In the deep basin of the SCS, Guan et al. (2014) and Liu et al. (2018) detected harmonic waves with frequencies of inertial plus tidal motions. They believe these waves are produced by the nonlinear interaction between near-inertial and diurnal tidal waves.

Due to a lack of simultaneous cross-slope observations, no efforts have been made to examine the cross-shelf variation of storm-induced NIOs over the slope of the SCS. Based on 3 years records of currents and winds measured on an array of moored current meters and meteorological buoys, Chen et al. (1996) examined the cross-shelf structure of wind-generated NIOs over the LATEX shelf. They found that in addition to the surface-intensified, first mode structures, the near-inertial energy had the maximum at the shelf break, decaying gradually toward the coast but rapidly offshore. Through numerical experiments with a primitive equation model, Chen and Xie (1997) found that as cold-fronts passed, the NIOs excited over the shelf can propagate toward the shelf break. The resulting slope-intensified NIOs are under a balance of the cross-shelf gradient of surface elevation and vertical gradient of Reynolds stress. A similar slope-intensified feature was observed in near-inertial waves over the Tasmanian shelf Australia by Schlosser et al. (2019). They found that the inertial energy can be trapped over the slope by the subtidal flow with negative vorticity.

Over the continental slope, a subtidal flow with negative vorticity, that is, an anticyclonic eddy, can cause a frequency shift of NIOs and traps the inertial energy in a negative vorticity zone (Kunze and Sanford, 1984; Kuze, 1985; Jaimes and Shay, 2010). In addition, the wind-driven coastal trapped waves prevail over the continental shelf (Brink et al., 1987; Brink & Chapman, 1985). These waves are upbounded at an inertial frequency, and their amplitudes vary with topographic slope (Brink, 1980). The near-inertial waves propagate along the shelf as coastal-trapped waves, with maximum energy trapped at the shelf break (Brink & Chapman, 1985). Chen and Qin (1985) examined the response of subtidal flow to a storm-induced wind in a finite-depth idealized ocean. They found that after the storm passes, the flow undergoes an adjustment process, during which the storm-generated energy is dispersed through an energy transfer from the low-frequency flow to the inertial motion.

An array of eight moored current meters and two meteorological buoys was deployed within major pathways of TCs across the northern shelf of the SCS from September 1, 2017 through September 30, 2018. Three TCs, Khanun, SonTinh, and Mangkhut, traversed by the storm-monitoring array in October 2017, July, and September 2018, respectively (Figure 1). These moorings captured the cross-shelf structures of inertial,

Table 1
Depth, Time, Instrument, and Sampling Spatial and Time Intervals of Acoustic Doppler Current Profilers Measurements

		ADCP					
Station	Depth (m)	Number	Frequency (kHz)	Bin length (m)	Time interval (min)	Vertical coverage (m)	Time coverage
M1	546	2	150	8	10	34–522	January 7–September 30, 2018
M2	186	2	300	4	10	17–176	September 1, 2017–September 30, 2018
M3	114	2	300	4	10	11–110	September 1–December 1, 2017 March 19-August 4, 2018
M4	76	2	300: up 600: down	4: up 2: down	10	17–67	September 1–November 23, 2017 June 23–August 6, 2018

tidal, and subtidal frequency flows. Using these data, we examined the cross-shelf and vertical structures of NOIs over the northern shelf of the SCS. Do TC-generated NIOs over this shelf have a slope-intensified feature like those observed over the LATEX and Tasmanian shelves? Do the NIOs produce a significant interaction between near-inertial and tidal currents? How do NIOs vary in the vertical through the thermocline? What are the contributions of low-frequency flow to the evolution and cross-shelf energy distribution of NIOs? To our knowledge, these questions have not been well explored over the northern shelf of the SCS.

This study will address these questions by synthesizing the observational data received from an array of moored current meters and meteorological buoys, hydrographic surveys, and satellite-derived sea surface height (SSH) fields. The remaining sections are organized as follows. In Section 2, the in situ data are described. In Section 3, the major observed features are presented. In Section 4, the possible physical mechanisms for slope-intensified NIOs are discussed. In Section 5, the conclusions are summarized.

2. In situ Data

An array of moored current meters and meteorological buoys were deployed with a layout across the depth range from 546 to 76 m over the northern shelf of the SCS (Figure 1). This array consisted of eight moored Acoustic Doppler Current Profilers (ADCPs) at sites of M1-M4 and meteorological measurement sensors (Wind Monitor-MA-Model 05106, Relative Humidity/Temperature Probe-Model-4138LC2, Air Pressure Senor-Model-QYX4-1) at buoys B1 and B2. Moored ADCPs were deployed on September 1, 2017, and remained in the water until September 30, 2018. On each mooring, a pair of up and down-looking ADCPs were mounted at the middepth, respectively. The working frequency, bin length, sampling time interval, spatial and time coverages of ADCPs are listed in Table 1. Due to interference by fishing activities and storm damages, the ADCP signals at sites M1, M3, and M4 were lost during some storm crossing periods. For Mangkhut, the maximum tilt of ADCPs at M2 exceeded 15°. The signals received during that period were too noisy to be used. A 3 h low-passed Lanczos filter was used to convert the current data to hourly interval records (Chen et al., 1996). Buoys B1 and B2 were deployed in 2015 as a component of the SCS buoy observation network program. The wind speed and direction were recorded with an hourly interval in general and increased to 30 min during storms. Unfortunately, the wind sensor on Buoy B2 was destroyed on June 1, 2018. We compared the WRF-predicted wind speed and directions with data available on Buoy B1 and B2 and found that they were in good agreement with a correlation coefficient of ~0.9 and root mean square errors of 0.5–3.7 m/s during the storms (Figure 2). Since either Buoys B1 or B2 had some distances from moorings, we used the WRF-predicted winds at the mooring site for our analysis.

Three hydrographic surveys were conducted across the northern shelf of the SCS on November 17, 2017, May 13, and September 23, 2018, respectively (Figure 1). According to findings from recent observations over the northern shelf of the SCS, the adjustment time of temperature in this tropical region after a storm is generally about a week (Dong et al., 2020). We used observed temperature profiles from the CTD measurements to compare the vertical distribution of near-inertial energy observed during storms, assuming that these profiles represented vertical stratification during those seasons.

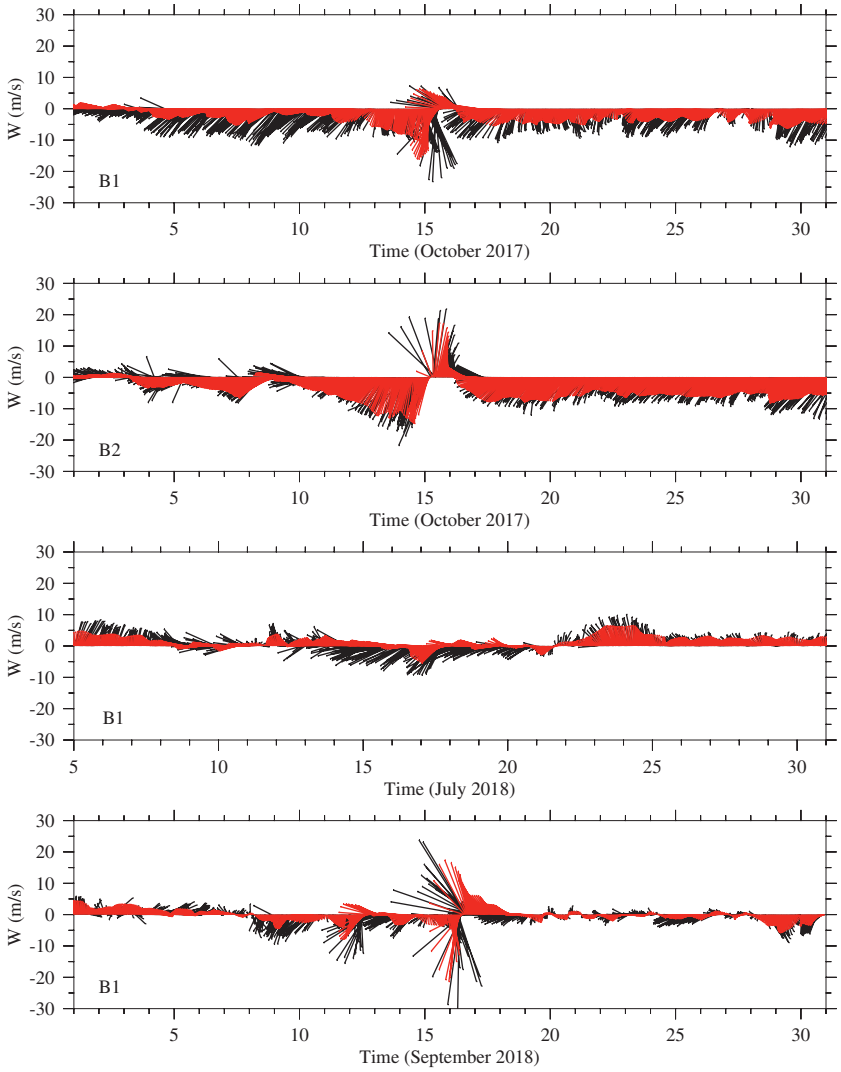

Figure 2. Comparisons between observed and WRF-Simulated wind vectors at the 10 m height on buoys B1 and B2. Black vectors: Observed. Red vectors: WRF-simulated.

A band-passed filter was used to construct the time series of near-inertial currents at each mooring site. The band was defined as (1.0 ± 0.1) × local inertial frequency, which were the same as those used in previous literature (Chen et al., 1996; Pollard, 1970; Sun, Zheng, et al., 2011). The band frequency range was 0.623–0.761 cpd for M1, 0.624–0.763 cpd for M2, 0.633–0.774 cpd for M3, and 0.650–0.794 cpd for M4. The study area is around 19°N–21°N over the SCS shelf, with local inertial periods of 33.39–36.76 h. Over the northern shelf of the SCS, K_1 and O_1 are two dominant diurnal tidal constituents with periods of 23.93 and 25.82 h, respectively. The differences between local inertial and diurnal tidal periods are at least 7.57 h, so that a band-passed filter works very well to separate the inertial and diurnal tidal energies (see a more discussion in Section 3). The tidal analysis was done using the MATLAB Tidal Analysis Toolbox (Pawlowicz et al., 2002). The PL64 low-passed filter was used to construct the 40 h low-passed subtidal currents (Beardsley et al., 1985).

We downloaded the satellite-derived maps of absolute dynamics topography and corresponding absolute geostrophic currents from the Archiving, Validation, and Interpretation of Satellite Oceanographic (AVSIO) database (http://www.aviso.oceanobs.com). These maps' spatial resolution is 1/4° × 1/4°, and the temporal resolution is one day. We used these data to examine the regional barotropic circulation during the storms. A comparison was also made with observed currents at the moorings.

Khanun entered the SCS as a TC with a maximum wind speed of ~18 m/s on October 13 (Figure 1). It was rapidly intensified to be a typhoon with a maximum wind speed of ~42 m/s on October 15, passed the mooring sites M1-M3 on the left, and then moved toward the coast. SonTinh was much weaker than Khanun. It entered the SCS as a TC with a maximum wind speed of ~15 m/s on July 17 (Figure 1). This TC slightly intensified on its journey toward Hainan Island, with the shortest distance of ~99 km to the site of M1. Mangkhut entered the SCS as a severe typhoon with a maximum wind speed of ~50 m/s on September 15 (Figure 1). This typhoon passed the mooring array on the right on September 16, with the wind intensity much stronger than Khanun.

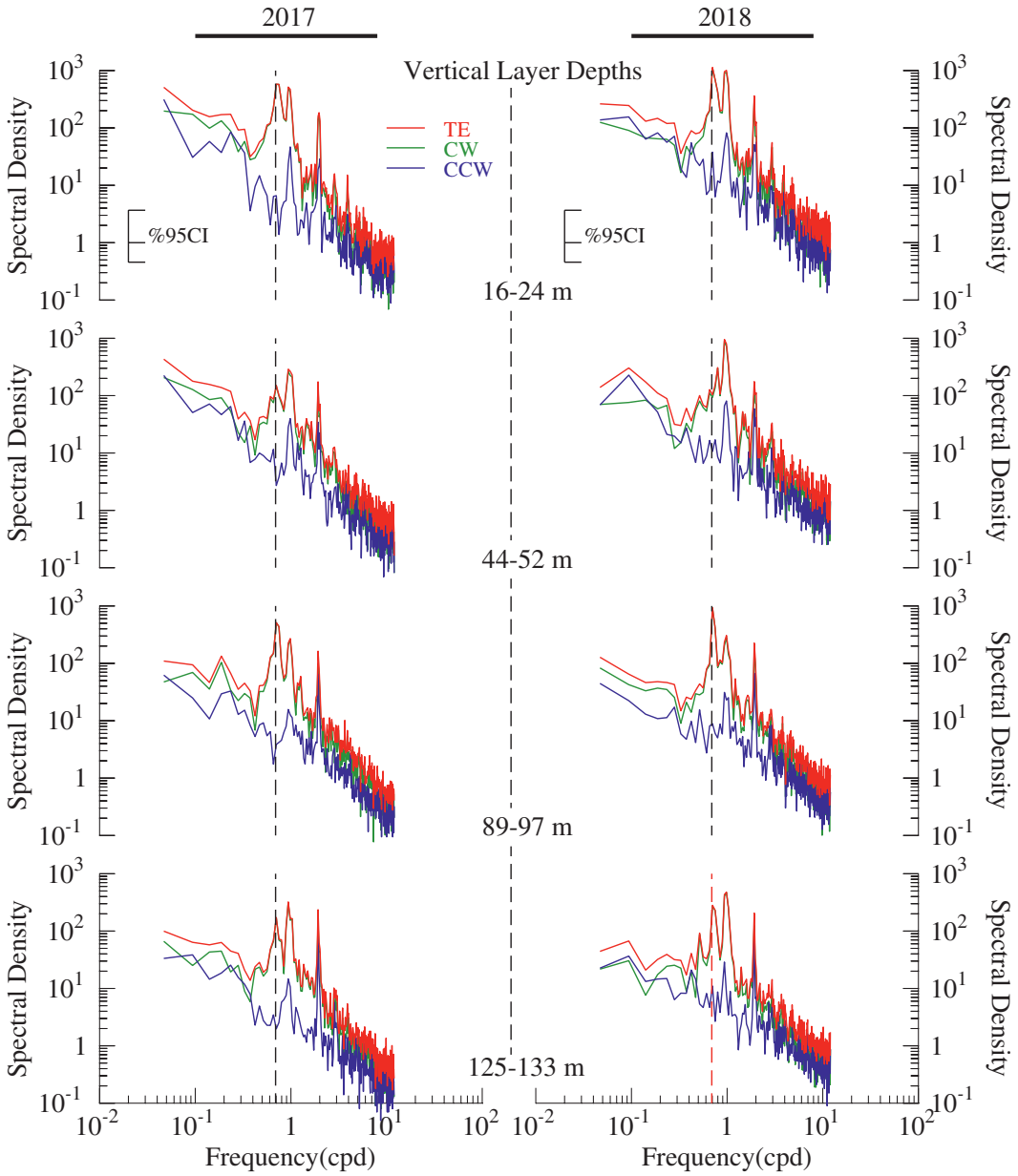

Figure 3. Spectral densities calculated by the velocity averaged in layers of 16–24, 44–52, 89–97, and 125–133 m at site M2 over September–November 2017 and July–September 2018. CW: Clockwise, CCW: Counterclockwise. A 95% confidence interval is drawn in the top panels.

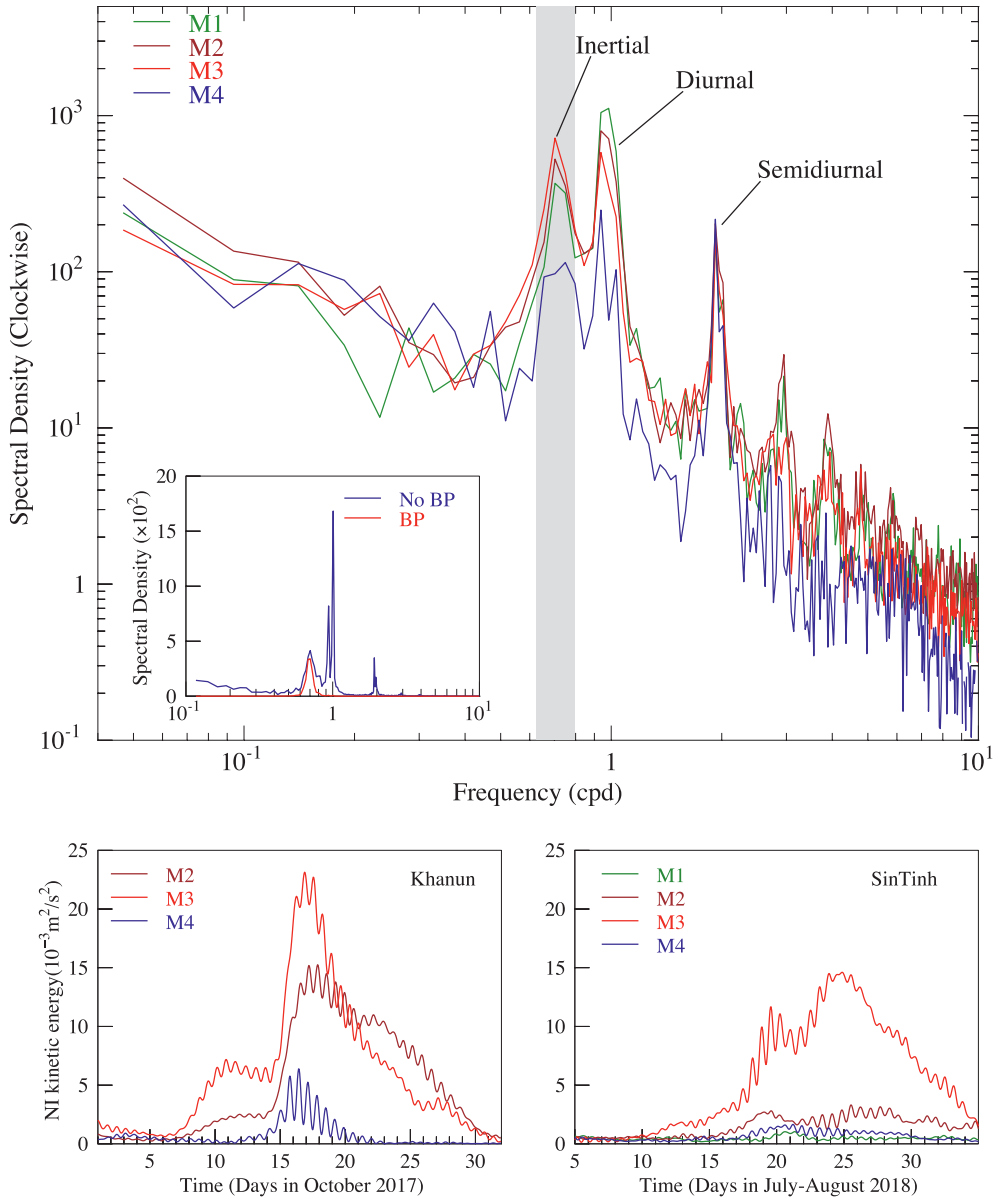

Figure 4. Upper panel: Clockwise spectral densities in the upper 34 m layer calculated with available hourly time-series records at sites M1, M2, M3, and M4. The gray shadow indicates the frequency band used for the band-passed filter. A figure inserted in the upper panel provides a comparison between the spectral energies obtained using the methods with and without a band-passed filter. BP: band-passed, No BP; no band-passed. Lower panels: The change of the near-inertial kinetic energy with time at sites M2, M3, and M4 during the Khanun crossing period (left) and at sites M1, M2, M3, and M4 during the SonTinh crossing period (right).

3. Results

Rotary spectral densities were calculated using available current records over September–November 2017 and July–September 2018, respectively. The frequency resolution was 0.0469 cpd, and the degree of freedom was 8. The results show that the northern shelf of the SCS was predominated by near-inertial, diurnal, and semidiurnal tidal energies (Figures 3 and 4). The NIOs and diurnal tides were dominated by clockwise motions, while the semidiurnal tides did not (Figure 3). Both near-inertial and tidal energies varied significantly across the shelf. The clockwise spectral densities of the near-surface kinematic energy at sites M1, M2, M3, and M4 indicated that the diurnal tidal energy was generally larger than the near-inertial and

semidiurnal tidal energies, with its magnitude increasing monotonically across the shelf, smallest at site M4 and largest at site M1 (Figure 4: upper panel). Differing from diurnal tidal currents, the near-inertial energy exhibited a slope-intensified feature, with its maximum at shelf break (M3) and decaying offshore (M2 and M1) and onshore (M4), respectively. The slope-intensified feature of NIOs was highlighted on the cross-shelf distribution of vertically averaged, band-passed near-inertial kinetic energy during the Khanun and SonTinh crossing periods on October 15–28, 2017 and July 18–29, 2018, respectively (Figure 4: lower panels), and also the time-averaged kinetic energy over these two periods in Figure 5. Although Khanun and SonTinh significantly differed in intensities and trajectories, the NIOs excited by these two storms all exhibited a slope-intensified feature with the maximum energy near the site M3. A comparison was made between the spectral densities for the cases with and without band-passed filtering. The results show that the band-passed filter used in this study was robust to filter the diurnal tidal energy with no significant sacrifice at the near-inertial energy (Figure 4: in the upper panel).

In addition to the slope-intensified feature, the storm-induced NIOs over the northern shelf of the SCS were characterized by a vertical structure different from the first baroclinic mode described in Chen, et al. (2015) and Yang et al. (2015). In the first baroclinic mode, the near-inertial energy has its maximum at the surface and bottom. Our observations show that the NIOs were excited near the surface when the wind suddenly changed its direction (Figure 6). The oscillation energy rapidly transferred downward and caused the same frequency oscillations in the deeper region. The maximum amplitude of deep NIOs was at or close to the bottom (Figures 5 and 6). At site M2, for example, for Khanun, the strong NIOs first appeared in the upper 40 m mixed layer around October 15, then the oscillations started 4–5 h later in the lower layer below a depth of 60 m (Figure 6: left panels). The energy of deep oscillations predominated in the lower layer between 70 and 130 m, even though it reached the bottom at the beginning. There was a clear energy transition zone at depths of 40–60 m between the upper and lower layers. Similar features were also found at site M2 in Mangkhut (Figure 6: middle panels). In both cases, the thickness of the transition zone remained unchanged with time. The difference was that the transition zone deepened with time during the Mangkhut crossing period, while it remained stable during the Khanun crossing period. It was clear that the downward energy transfer was related to wind strength. Stronger wind in Mangkhut produced a faster downward energy transfer. As a result, the maximum oscillations in the lower layer occurred almost simultaneously with the oscillations in the upper layer. For SonTinh, the NIOs was strongest at site M3, with maximum energy occurring around July 24–25 after a sudden change in the wind direction (Figure 6: right panels). The downward transfer of the near-inertial energy was also evident at this site, with a transition zone at depths of 30–40 m between the upper and lower layers. Although SonTinh was far away from the mooring array and the wind was much weaker, it still generated the same order of magnitude NOIs as Khanun and Mangkhut.

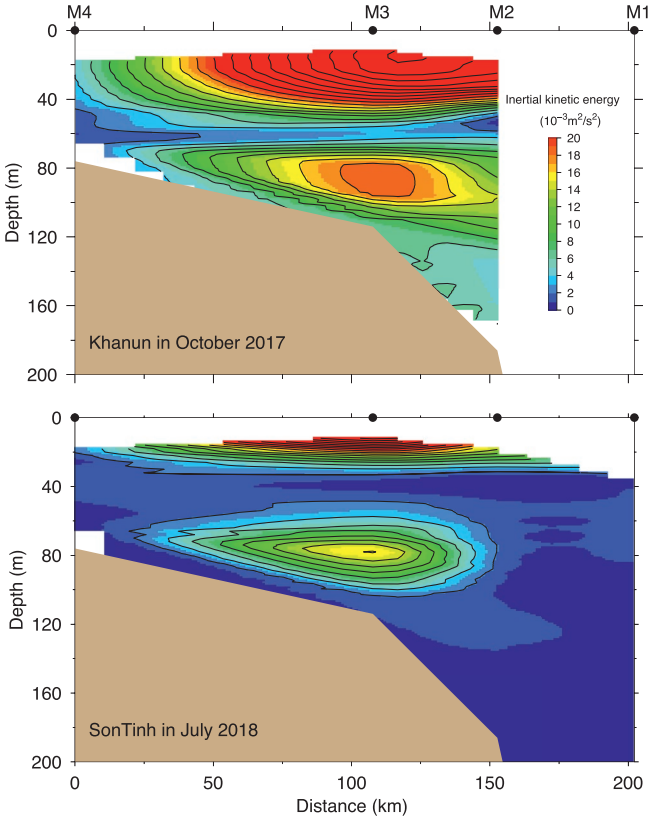

Figure 5. Cross-shelf distributions of the near-inertial oscillation energy averaged over September 15–28 2017 for Khanun and July 18–29, 2018 for SonTinh, respectively. Image color scales used in SonTinh were the same as those used in Khanun.

During summer through fall, the northern shelf of the SCS was stratified, with a thickness of the surface mixed layer in the range of ~30–50 m (Dong et al., 2020). The three hydrographic surveys were conducted on the same transect two weeks after Khanun, two months before SonTinh, and a few days after Mangkhut. The cross-shelf distributions of the temperature and Brunt-Väisälä frequency (N) on that transect for those three cruises are shown in Figure 7. In the deep region, the maximum N remained at depths of 50–60 m in May and September 2018, while it was around 80 m in November 2017. The vertical stratification was weaker around Khanun than around Mangkhut and SonTinh. Over the shelf, the water was well mixed in November 2017, while it remained stratified in May and September 2018. The vertical structures of storm-generated NIOs were associated with the vertical profile of water density. The transition zone of the amplitude and phase of the oscillations between the

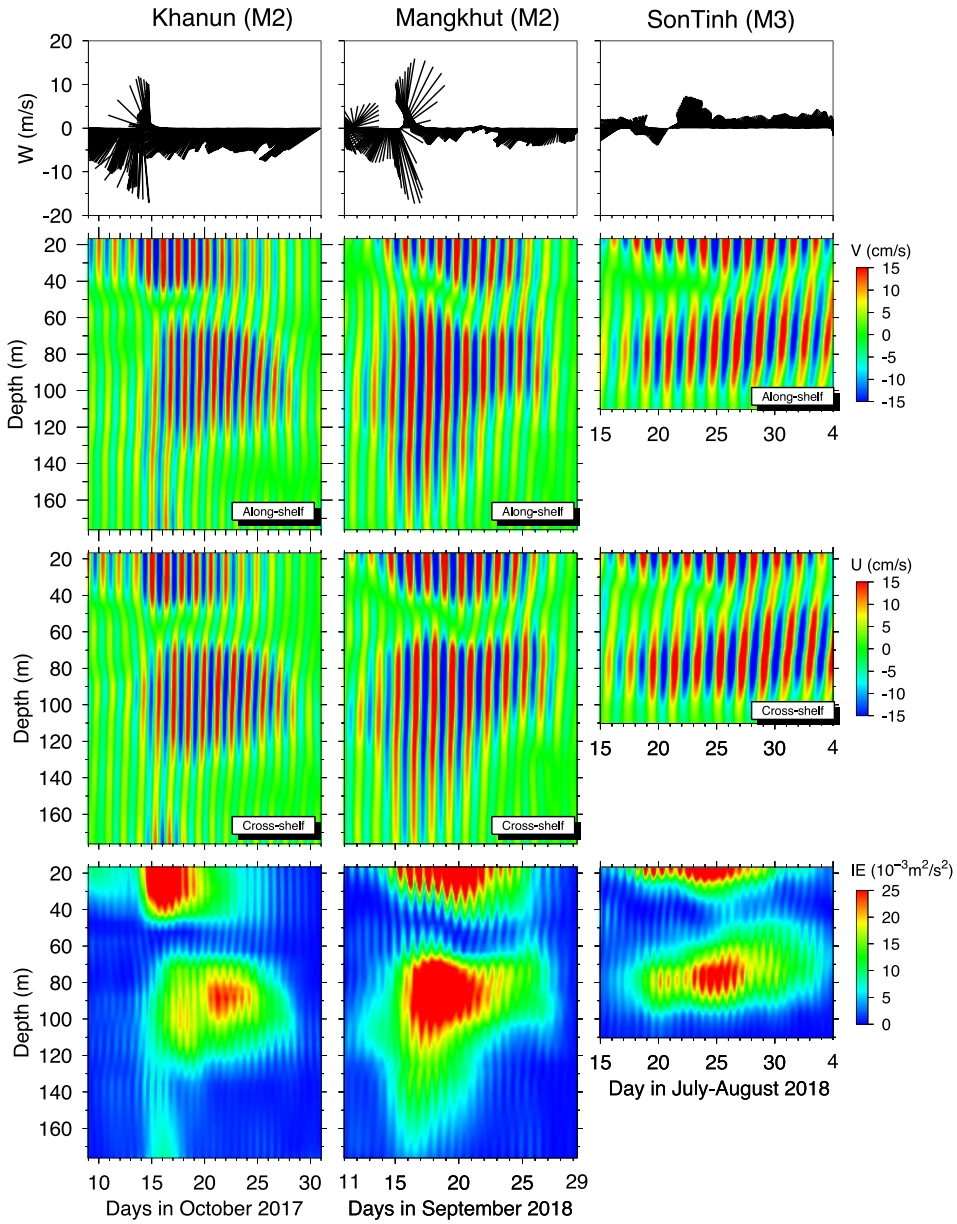

Figure 6. Time series of the wind vector at a 10 m height, along-shelf and cross-shelf near-inertial currents, and near-inertial energy at site M2 during the Khanun and Mangkhut crossing periods and at site M3 during the SonTinh crossing period, respectively. W: the wind velocity. V: the water velocity. NIE: near-inertial energy.

upper and lower layers matched well with thermoclines. For Khanun, at site M3, the NIOs were strong in the upper mixed layer, decreased rapidly through thermoclines, and increased again at depths of ~75–95 m in the lower stratified layer (Figure 8: upper-left panel). Correspondingly, the oscillation phase changed significantly through thermoclines, with a maximum difference of ~140° between upper mixed and lower stratified layers. At site M4, the water was relatively mixed throughout the water column with a relatively weak density gradient at depths of ~40–45 m. The NIOs were relatively uniform throughout the water column with small amplitude and phase changes in the relatively large density gradient layer (Figure 8: lower left panel). The maximum differences between the surface and bottom were ~3.0 × 10^{-3} m^2/s^2 in amplitude and ~15° in phase. Similar features were also found during the SonTinh crossing period. The stratification was stronger in July 2018, compared with October 2017. At site M3, the NIOs decreased as the density increased with depth, reached a minimum at depths of ~30–45 m within the greatest density

gradient layer, and became significant again at depths of ~70–80 m in the lower stratified layer (Figure 8: upper-right panel). The oscillation phase also showed a substantial change through thermoclines with a maximum difference of ~180° between upper and lower stratified layers. At site M4, although stratification was not as strong as that at site M3, N was in an order of magnitude of 10^{-2} s^{-1}. The oscillation phase changed rapidly with depth in the upper 20 to 30 m layer, even though the amplitude decreased with depth in general (Figure 8: lower right panel). The maximum phase difference between the upper and lower layers reached ~160°.

We conducted a tidal harmonic analysis to construct the diurnal and semidiurnal tidal currents. Time series records show that the diurnal tidal energy varied with season, stronger in spring through early fall and weaker in late fall through winter (Figure 9). During the fall season, the semidiurnal tidal currents were generally one order of magnitude smaller than the diurnal tidal currents (Figure 9). The diurnal tidal currents were much stronger during the SonTinh crossing period than during the Khanun crossing period, even though the along-shelf distribution patterns of the tidal kinetic energy in the upper 40 m layer remained the same during these two periods (Figure 10). The semidiurnal tidal currents were bottom-intensified during the Khanun and SonTinh crossing periods. The bottom-intensified feature was observed in the diurnal tidal currents during the SonTinh crossing period but not during the Khanun crossing period (Figure 10).

We also observed the harmonic waves with frequencies of $f \pm \omega_d$ and $f + \omega_{sd}$ (f is the local inertial frequency, ω_d and ω_{sd} are the diurnal and semidiurnal tidal frequencies, respectively) (Figure 11), which were similar to those reported in the other region of the SCS by Guan et al. (2014) and Liu et al. (2018)Since these harmonic waves appeared within a short-time period during the storm crossing period, they were not resolved in spectral densities at different depths (Figure 3). The kinetic energy of harmonic waves varied among the three TCs. The harmonic waves with frequencies of $f \pm \omega_d$ were more significant during the Khanun and Mangkhut crossing periods than during the SonTinh crossing period (Figure 11). Similar features were also found for harmonic waves at frequencies of $f \pm \omega_{sd}$. The harmonic waves at a frequency of $f - \omega_{sd}$ was in the same order of magnitude as the harmonic waves at a frequency of $f + \omega_d$ (Figure 11).

We estimated the nonlinear tidal and inertial advection terms using the observed current data at sites M2 and M3 and compared them with the Coriolis force terms. The results show that they were at least two orders of magnitude smaller, suggesting that the nonlinear interaction between near-inertial and tidal cur-

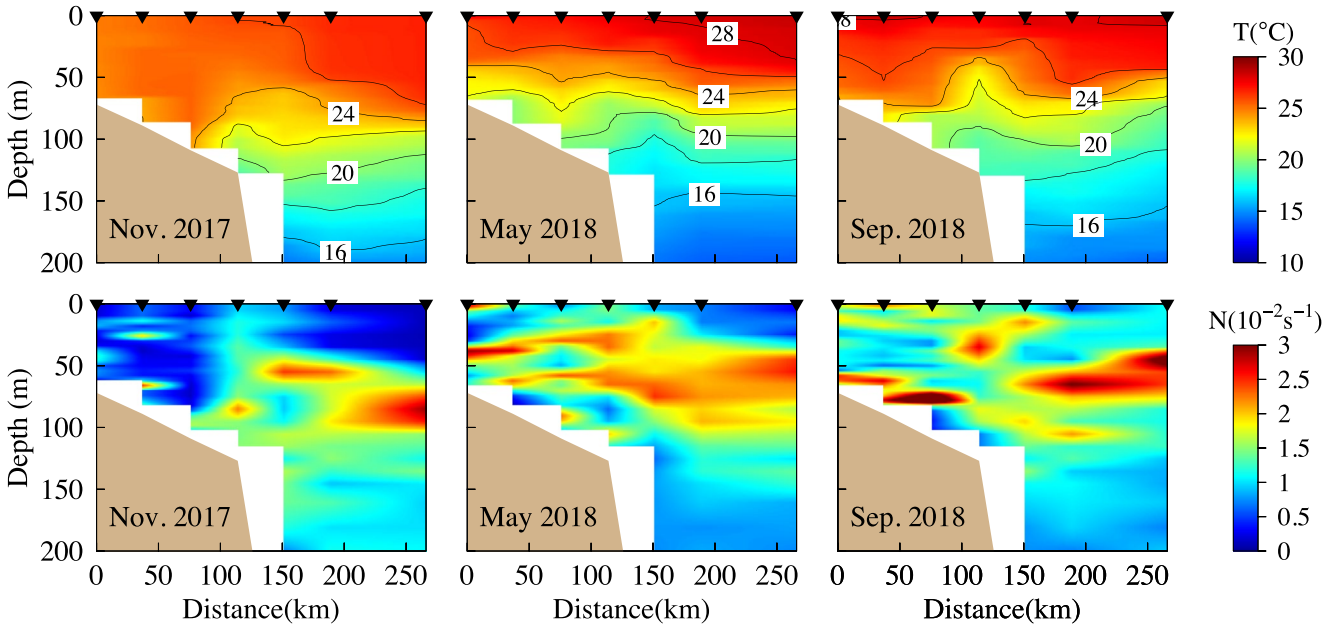

Figure 7. Cross-shelf distributions of water temperature (upper panels) and Brunt-Väisälä frequency (N) (lower panels) on a CTD transect taken during the hydrographic surveys on November 17, 2017, May 13, and September 23, 2018, respectively. Filled down-triangles: the CTD station locations (the latitude and longitude of each station are given in Figure 1).

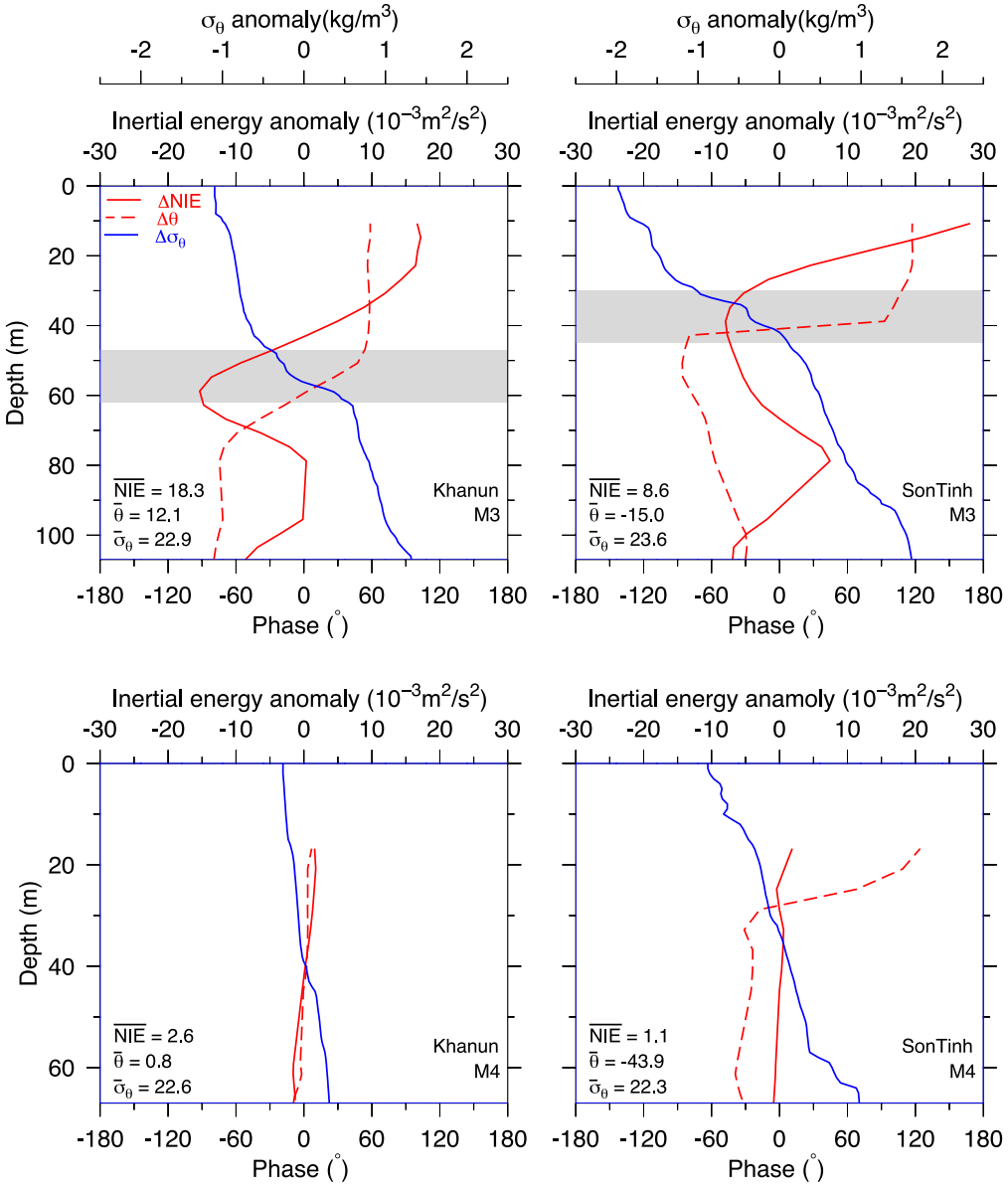

Figure 8. Vertical profiles of density anomalies, near-inertial energy anomalies, and phases at site M3 (upper panels) and M4 (lower panels) for Khanun (left) and SonTinh (right). NIE: near-inertial energy. θ: Phase. σ_θ: the potential density with a reference at the sea surface. Superscript indicates the vertically averaged mean. Definitions of curve colors in each figure were the same used in those shown in the lower-left panel. The anomaly was calculated relative to the vertical mean value.

rents were too small to be accountable. Meanwhile, the NIO amplitude was not correlated to the strength of tidal currents (Figure 12). At site M2, for example, the diurnal tidal currents had similar amplitudes during the Khanun and SonTinh crossing periods, but the NIOs were much stronger during the Khanun crossing period than during the SonTinh crossing period. During the Mangkhut crossing period, the strong NIOs lasted about ~10 days, appearing around September 15 and reached a maximum around December 20. During this period, the diurnal tidal currents were weaker compared with Khanun and SonTinh cases. The diurnal tidal amplitude varied significantly with time, undergoing two peaks on September 17 and 20, respectively. The tidal variation was not correlated to the temporal change of NIOs.

Alford (2001b) examined the "fine-structure contamination" of the velocity measurement at a fixed depth due to Doppler shift by the vertical advection. He found that at low-latitude, the heaving of isopycnal lay-

ers could result in velocity peaks at $f \pm \omega_d$. This advective error has no dynamically meaning and should be removed using an isopycnal-following coordinate. This type of Doppler shift was also reported in the near-inertial wave measurements in the Luzon Strait of the SCS by Le Boyer et al. (2020). Since no advective calibration was made for our current measurements, we believe that the harmonic waves shown in Figure 11 resulted from the Doppler-shifted errors.

Over the slope of the northern shelf of the SCS, the low-frequency current was predominated by a southwestward along-slope flow. This flow was significantly intensified during the storm crossing period: up to ~4 cm/s for Khanun (Figure 13) and SonTinh (Figure 14). The storms also intensified the onshore flow by ~4–8 cm/s in the upper 60 m layer during the Khanun and SonTinh crossing periods. The along-slope flow was stronger during the SonTinh crossing period than during the Khanun crossing period. The observations reveal that in all three TC cases, the strongest NIOs occurred during an adjustment period of the low-frequency currents restoring to a prestorm condition (Figure 12), implying that after the NIOs were excited, there was an energy transfer from the low-frequency flow to NIOs, like the process described in Chen and Qin (1985).

To examine the energy transfer of the low-frequency flow to the near-inertial motions, we first estimated the contribution of nonlinear advection terms of $\partial\overline{\left(u_L KE_I\right)} / \partial x$ and $\partial\overline{\left(u_I KE_L\right)} / \partial x$ to the local change of KE_{I}, where KE_{I} is the inertial kinetic energy, u_{L} and u_{I} are the low-frequency and near-inertial currents, respectively, x is the cross-shelf axis, and the superscript "–" represents a vertically average sign. The results show that these two terms are too small to be accountable for the local change of KE_{I}. Assuming that the along-slope flow is quasigeostrophic under a pre-storm condition, we could estimate the energy transfer from the low-frequency flow to the inertial motion by a simple linearized equations given as

$$\frac{\partial u}{\partial t} - fv = -\frac{1}{\rho_o}\frac{\partial P}{\partial x} \tag{1}$$

$$\frac{\partial v}{\partial t} + fu = 0 \tag{2}$$

where u and v are the cross- and along-shelf components of the velocity; P is the sea pressure; and ρ_{o} is the reference density. Under a quasigeostrophic approximation, we can define u and v as

$$u = u_{\mathrm{I}}; v = v_{\mathrm{I}} + V; \text{and } V = \frac{1}{f\rho_{\mathrm{o}}}\frac{\partial P}{\partial x} \tag{3}$$

Substituting (3) into Equations 1 and 2 yields

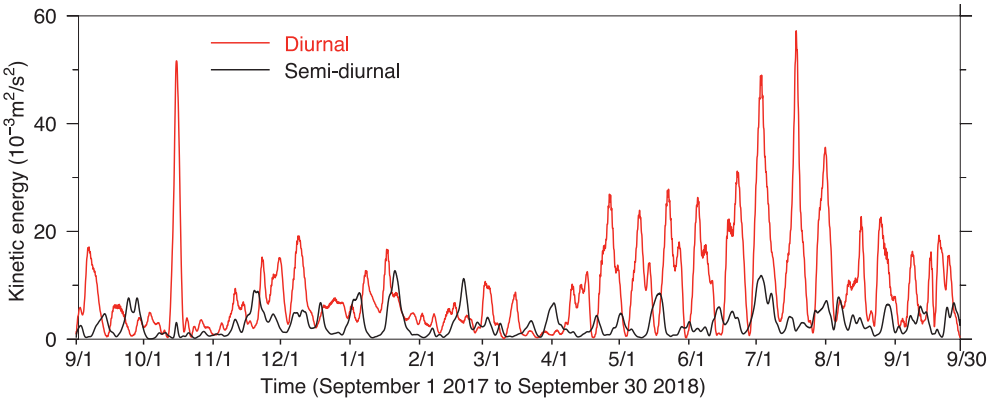

Figure 9. Time series of diurnal and semi-diurnal tidal kinetic energies near the surface at site M2 over September 1, 2017–September 30, 2017.

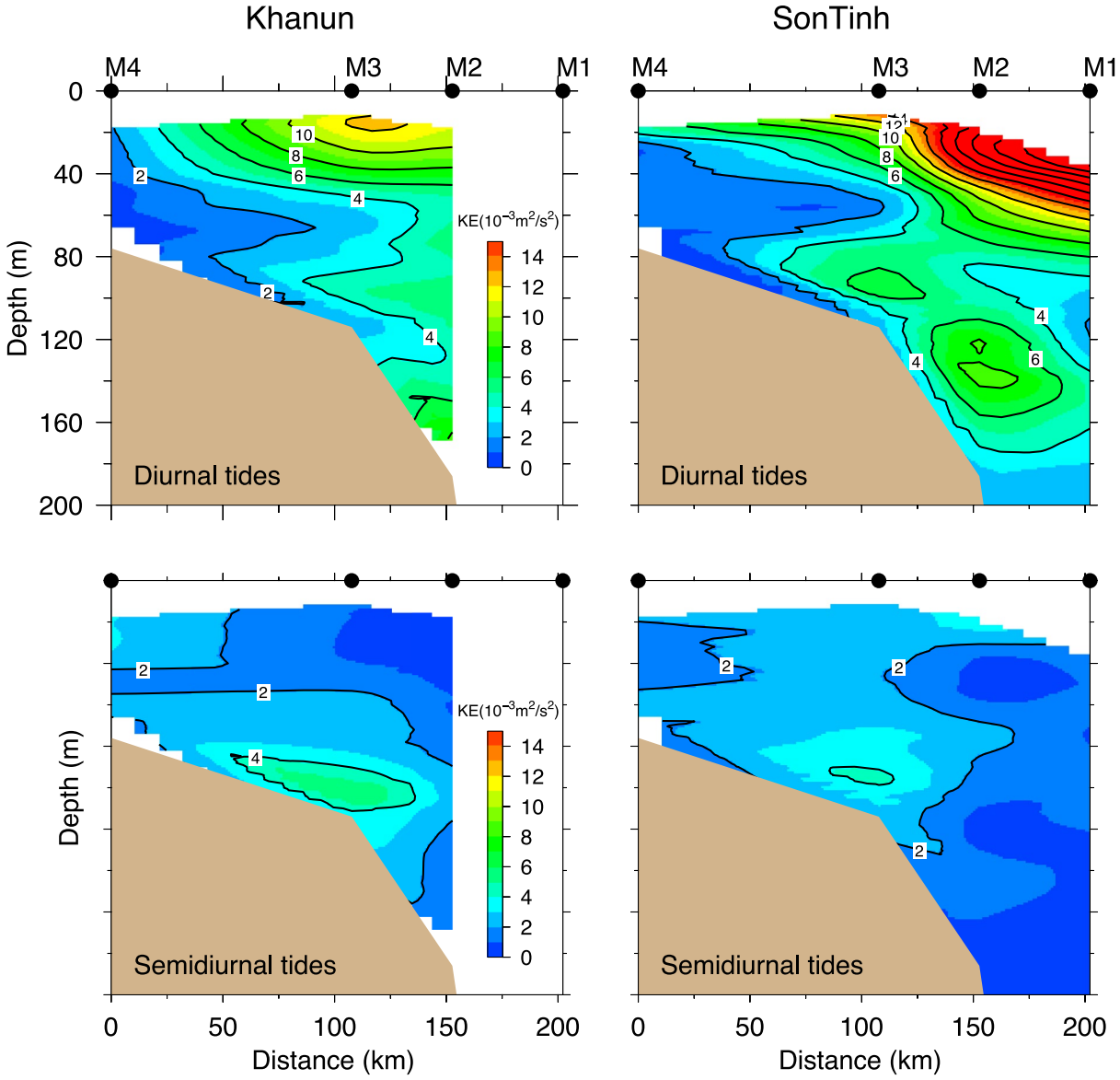

Figure 10. Cross-shelf distributions of diurnal and semi-diurnal tidal energies averaged over the periods of October 15–28, 2017 for Khanun and July 18–29, 2018 for SonTinh, respectively. Image scales for SonTinh were the same as those used for Khanun.

$$\frac{\partial u_I}{\partial t} - fv_I = 0; \frac{\partial v_I}{\partial t} + fu_I = -\frac{\partial V}{\partial t} \tag{4}$$

The near-inertial energy at the time t can be derived from (4), which is given as

$$E_{\mathrm{I}}(t) = E_{\mathrm{I}}(t_{\mathrm{o}}) - \int_{t_o}^{t}\int_{-H}^{0} v_{\mathrm{I}}\frac{\partial V}{\partial t}\mathrm{d}z\mathrm{d}t \tag{5}$$

where $E_I = \int_{-H}^{0} KE_I\, dz$ is the vertically integrated near-inertial energy. We estimated $E_I(t)$ at sites of M1, M2, M3, and M4 during the adjustment period of the low-frequency flow for the three TCs whenever the measurements were available. The results show that the maximum energy transfer from the low-frequency flow to the near-inertial motion occurred during the decreasing period of the low-frequency flow. An exam-

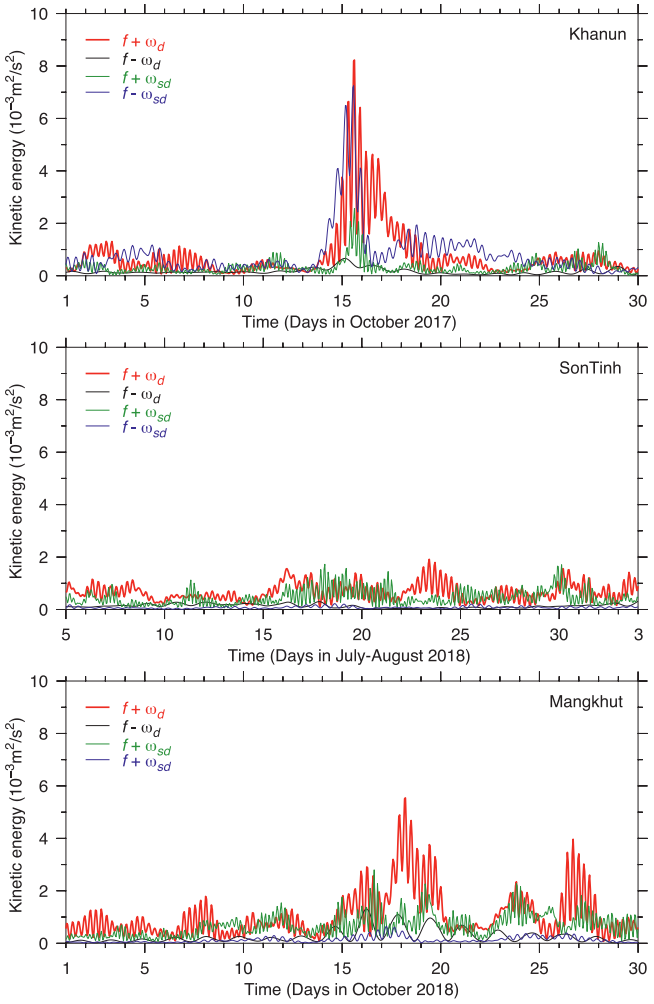

Figure 11. Time series of harmonic waves at frequencies of $f+\omega_d, f-\omega_d, f+\omega_{sd}$ and $f-\omega_{sd}$ that were produced by the nonlinear interactions between near-inertial and tidal motions at site M2 during the crossing periods of Khanun, SonTinh, and Mangkhut.

ple is shown in Figure 15 at site M2 for Khanun, SonTinh, and Mangkhut, which is consistent with Figure 12. This simple model demonstrates that over the slope of the SCS, after the NIOs is excited by the wind, there is an energy transfer from the low-frequency flow to the near-inertial motion through the flow adjustment process. It could explain why the maximum NIOs always occur during the decay period of the low-frequency flow after the storm passes.

Based on a scaling analysis of the kinetic equation for NIOs, the dissipation time scale (T_{diss}) of NIOs can be estimated by $T_{\text{diss}} \sim H^2 / 2K_{\text{m}}$, where H is the local water depth and K_{m} is the vertical eddy viscosity. Taking the site M2 as an example, at $H \sim 200$ m, $T_{\text{diss}} \sim 23$ days for a given $K_{\text{m}} \sim 10^{-3}$ m^2/s^2 and ~ 2.3 days for $K_{\text{m}} \sim 10^{-3}$ m^2/s^2. At this site, the observed dissipation time scale was 10–15 days for Khanun, SonTinh, and Mangkhut, which was within the range of the time scale estimated by the scaling analysis.

4. Discussions

The slope-intensified structure of storm-induced NIOs over the northern shelf of the SCS was very similar to that caused by passages of low air pressure fronts over the LATEX shelf (Chen et al., 1996) and the Tasmanian shelf(Schlosser et al., 2019). It is likely to be a ubiquitous feature over the slope wherever wind-induced NIOs exist. Over the LATEX shelf, Chen and Xie (1997) found that the NIOs behaves like near-inertial waves to propagate toward the shelf break. The strong nonlinear advection of near-inertial currents can occur at the shelf break, which leads to the growth of the large near-inertial energy over there. We also estimated the contribution of nonlinear advection terms of the near-inertial motion to the local change of the near-inertial energy by calculating $\partial\left(u_I KE_I\right) / \partial x$ over sites M2 and M3 for Khanun and SonTinh. The results show that these terms are one or two orders of magnitude smaller, so that horizontal advection contributed little to the slope-intensified feature of NIOs over the slope of the SCS.

We believe that the slope-intensified feature is likely associated with rapid change in the sloping topography, vorticity-trapping at the shelf break, and low-frequency energy transfer to the inertial motion. Brink and Chapman (1985) developed a program for computing the properties of wind-induced coastal-trapped waves over the continental shelf. The program can be applied for various sloping bottom topography under both barotropic and baroclinic conditions, including the step bottom topography. The slope-intensified feature can be interpreted by an analytical solution of near-inertial waves over an idealized step-topographic shelf under both homogeneous and stratified conditions; a case of coastal-trapped waves with an upbound inertial frequency over steep bottom topography as described in Brink and Chapman (1985). Considering a linear, continuous stratified case over a step-topographic shelf, in which all variables do not change in the along-shelf direction (Figure 16). Driven by an impulse wind forcing at initial, the near-inertial motion can be trigged and governed by Equations 1 and 2 plus the following two equations given as

$$w = -\frac{\partial^2 P}{\partial t \partial z} / \rho_o N^2; N^2 = -\frac{g}{\rho_o}\frac{\partial \overline{\rho}}{\partial z} \tag{6}$$

$$\frac{\partial u}{\partial x} + \frac{\partial w}{\partial z} = 0 \tag{7}$$

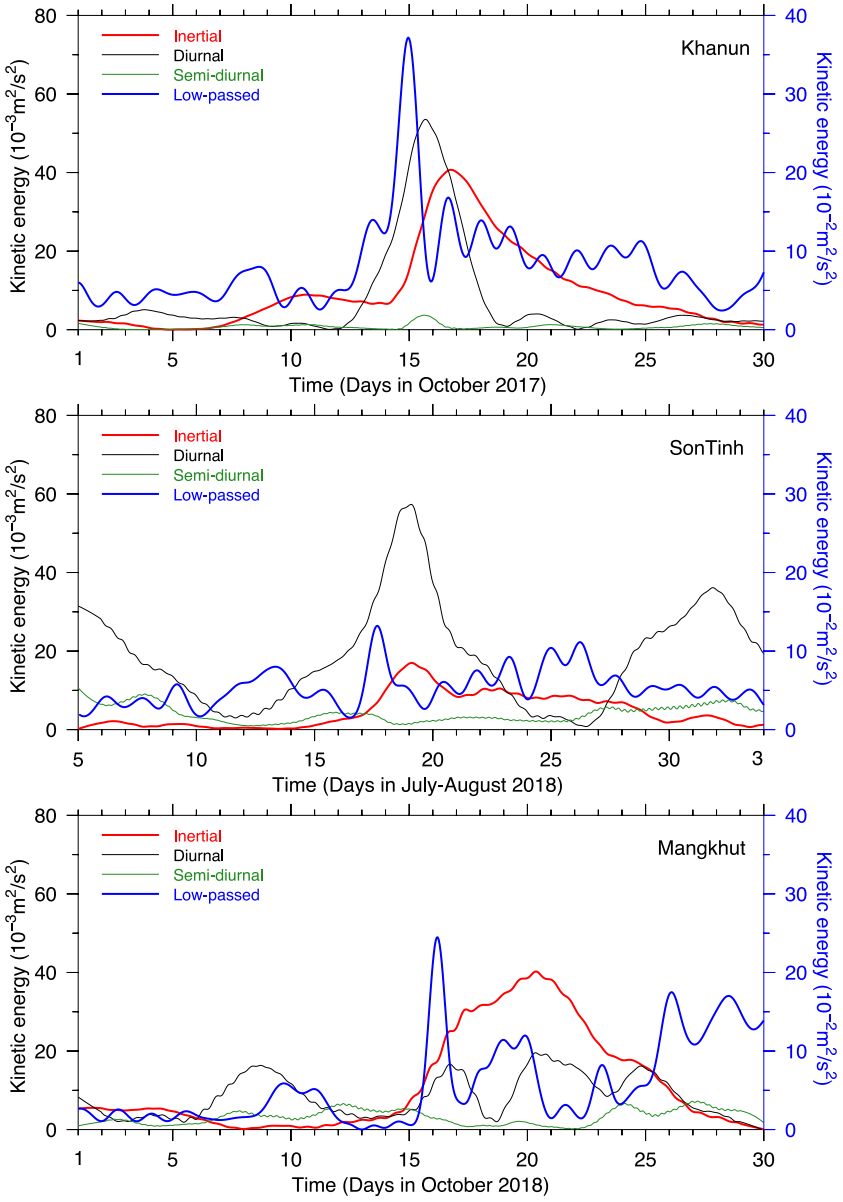

Figure 12. Time series of near-inertial, diurnal, and semidiurnal tidal, and the 40 h low-passed kinetic energies over October 1–30, 2017, July 5–August 3 2018, and September 1–30, 2018 for Khanun, SonTinh, and Mangkhut, respectively.

where z is the upward axis shown in Figure 16; w is the z-components of the velocity; ρ_o is the reference density; and $\overline{\rho}$ is the horizontally averaged densities. Defining all variables as the sum of low-frequency and inertial components like those in (3), a solution satisfying the boundary conditions of $u = 0$ at $x = 0$ and $\int_{-h}^{0} u_1 dz = \int_{-H}^{0} u_2 dz$ at $x = L$ (where subscripts "1" and "2" denote the shallow and deep regions where the water depths are h and H, respectively) can be derived from Equations 1–2 and 6–7 as follows:

$$u_1 = v_o \frac{f}{\omega} \frac{\mathrm{sh}\frac{x}{R_D}}{\mathrm{sh}\frac{L}{R_D}} \cos\frac{n\pi}{h} z \cdot \sin\omega t; v_1 = v_o \frac{\mathrm{sh}\frac{x}{R_D}}{\mathrm{sh}\frac{L}{R_D}} \cos\frac{n\pi}{h} z \cdot \cos\omega t, x \le L$$

$$u_{\mathrm{I}} = v_0 \frac{f}{\omega} e^{-(x-L)/R_{\mathrm{D}}} \cos\frac{n\pi}{H} z \cdot \sin\omega t; v_I = v_0 e^{-(x-L)/R_{\mathrm{D}}} \cos\frac{n\pi}{H} z \cdot \cos\omega t, x \geq L$$

where v_o is the velocity at $z = 0$ and $x = L$ at initial; $\omega \approx \pm f\sqrt{1-\left(\frac{1}{n\pi}\right)^2}$; n is an integer representing the vertical mode number of ≥ 1; and, R_{D} is the internal Rossby deformation radius defined as NH / f. This solution indicates that near-inertial oscillations excited by an impulse wind are slope-intensified with a maximum magnitude at shelf break and decays exponentially onshore and offshore over an e-folding cross-shelf scale, R_{D}, respectively (Figure 16). We also derived the solutions under homogenous and two-layer density conditions, and the slope-intensified feature remains. This feature is due to a sharp change of the bottom slope at which volume transports in the shallow and deep regions must be equal. This coastal-trapped wave result explains why the near-inertial energy remains high at the shelf break regardless of the trajectories and intensities of TCs were.

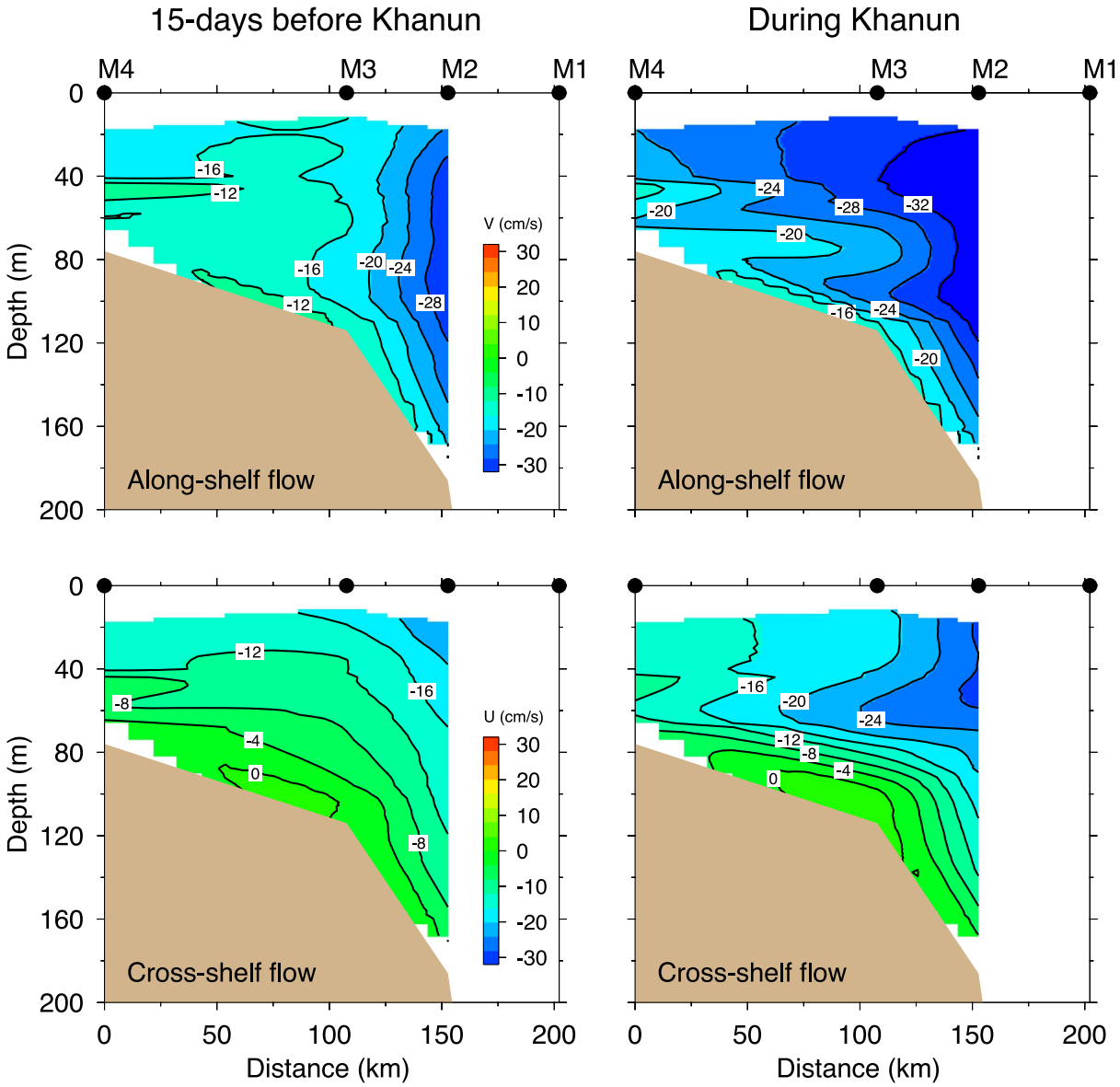

Figure 13. Cross-shelf distributions of the 40 h low-passed filtered along-shelf and cross-shelf currents 15 days before and during the Khanun crossing period.

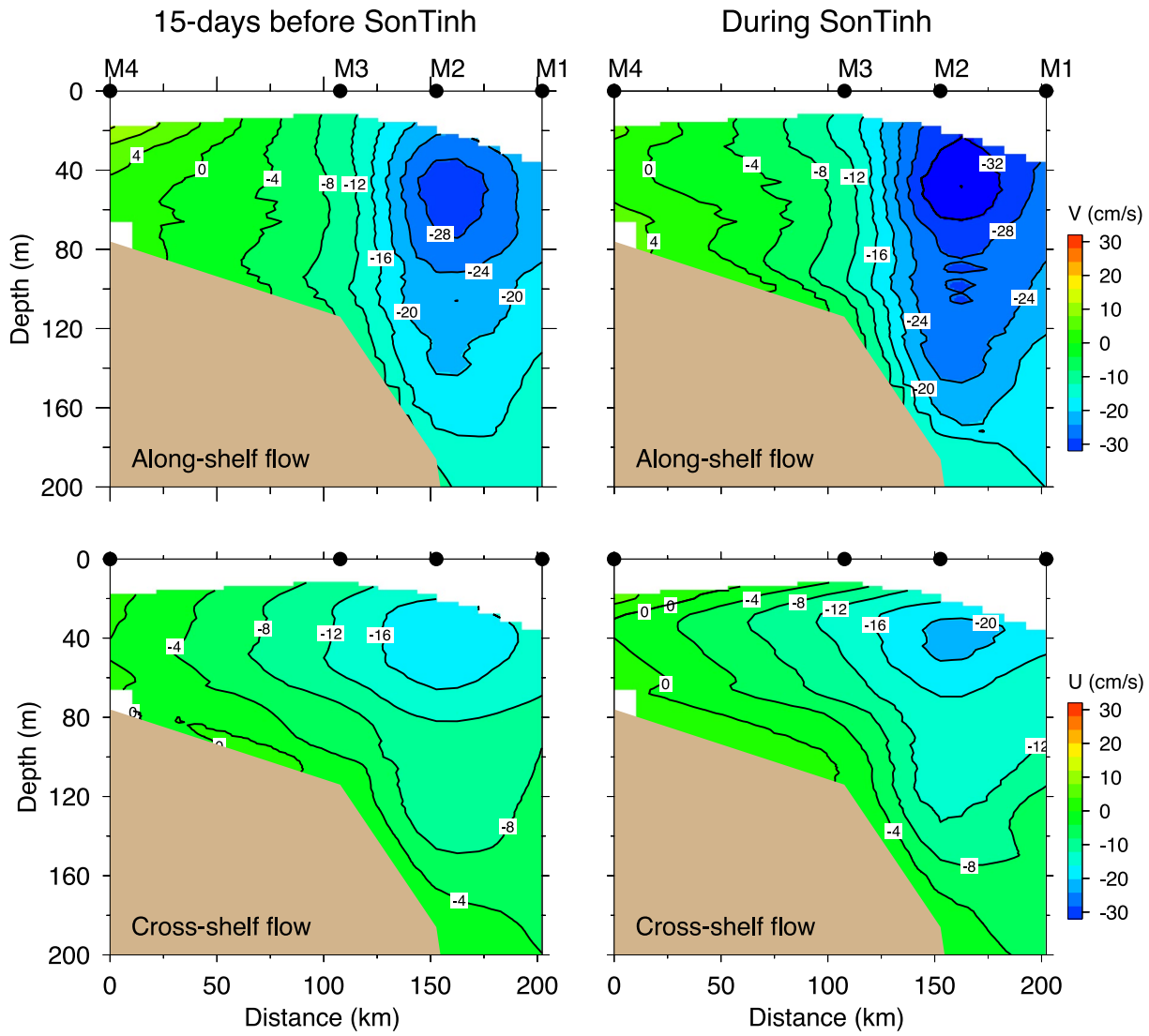

Figure 14. Cross-shelf distributions of the 40 h low-passed filtered along-shelf and cross-shelf currents 15 days before and during the SonTinh crossing period.

The mesoscale eddies are active over the slope of the SCS, which frequently appear around our study area (Li et al., 2014). These eddies were evident in the spatial distributions of the satellite-derived SSH and corresponded barotropic geostrophic circulation during the Khanun, SonTinh, and Mangkhut crossing periods. For example, on October 15, 2017, the southwestward flow was predominating over the northern shelf of the SCS, with a pair of anticyclonic and cyclonic eddies on the northeastern and southwestern sides of the mooring array (Figure 17: upper-left panel). These two eddies propagated southwestward along the slope during the Khanun crossing period. On October 23, the anticyclonic eddy arrived on the off-slope side of the site M1 (Figure 17: upper-right panel). On July 17, 2018, that site was occupied by a cyclonic eddy. At this time, the low-pressure center of SonTinh had already passed the mooring array on the south, with the shortest distance of >100 km from site M1 (Figure 17: lower-left panel). On July 24, 2018, the energetic NIOs still existed over the shelf. On that day, an anticyclonic eddy traveled through the mooring array (Figure 17: lower-right panel). We overlapped the observed daily averaged vertical mean velocity vectors on the satellite-derived absolute geostrophic velocity field. The observed and SSH-derived velocities were in good agreement (Figure 17).

We calculated the vorticity based on the gradient of the observed along-shelf velocities at the sites M2 and M3 for Khanun and SonTinh. An averaging was done for the vorticity over October 15–27, 2017 for Khanun

and July 17–31, 2018 for SonTinh. The result indicates that the strong NIOs occurred in a negative vorticity flow field for both Khanun and SonTinh. The negative vorticity was significantly larger during the SonTinh crossing period than during the Khanun crossing period (Figure 18). According to Kunze (1985)'s, the background vorticity can cause a frequency-shifting of NIOs or near-inertial waves with a value of ζ / 2, where ζ is background relative vorticity. We did observe a wider frequency range of NIOs in SonTinh than in Khanun, corresponding to a frequency-shifting range of 3.6%–5.6% for SonTinh and 0.4%–2.9% for Khanun (Figure 18). It suggests that more energy was transferred into the near-inertial motion during the SonTinh crossing period than during the Khanun crossing period.

According to the model result of Kunze (1985), the near-inertial waves can be trapped in a negative vorticity region because the freely propagating internal waves can exist only with a frequency range above the effective Coriolis frequency defined as $f + \zeta$ / 2. Since the largest negative vorticity occurred at the shelf break, the slope-intensified feature of NIOs could be a result of the energy trapped by a negative vorticity field. This also explains why the intensity of NIOs was stronger at the shelf break during the SonTinh crossing period than during the Khanun crossing period, even though the wind intensity was much weaker for SonTinh.

Comparing the vertical profiles of the negative vorticity and density shown in Figures 18 and 8, we found that the largest negative vorticity occurred beneath the main thermoclines. At site M3, for example, the main thermoclines were at depths of 50–60 and 30–45 m for Khanun and SonTinh, respectively. Correspondingly, the largest negative vorticity occurred at a depth of ~80 m for Khanun and ~50 m for SonTinh. The nonuniform distribution of the vorticity caused the frequency-shifting to vary in the vertical. The slope-intensified feature of NIOs in the lower stratified layer could also be trapped by the negativity vorticity field, even though the energy source was from the upper mixed layer. Since the mooring array only could resolve the cross-shelf structure, we do not know whether the near-inertial energy could propagate like the near-inertial internal waves. For this reason, we name it NIOs.

Our observations demonstrate a significant energy transfer from the low-frequency flow to NIOs during the slope flow adjustment to a pre-storm equilibrium state. A reasonable agreement between the observed vertically averaged and SSH-derived geostrophic velocity vectors (shown in Figure 17) suggests that as a first-order approximation, the along-shelf flow was quasigeostrophic before and after the storms. The flow adjustment to a pre-storm quasigeostrophic state could lead to the NIOs' energy accumulation at the shelf break.

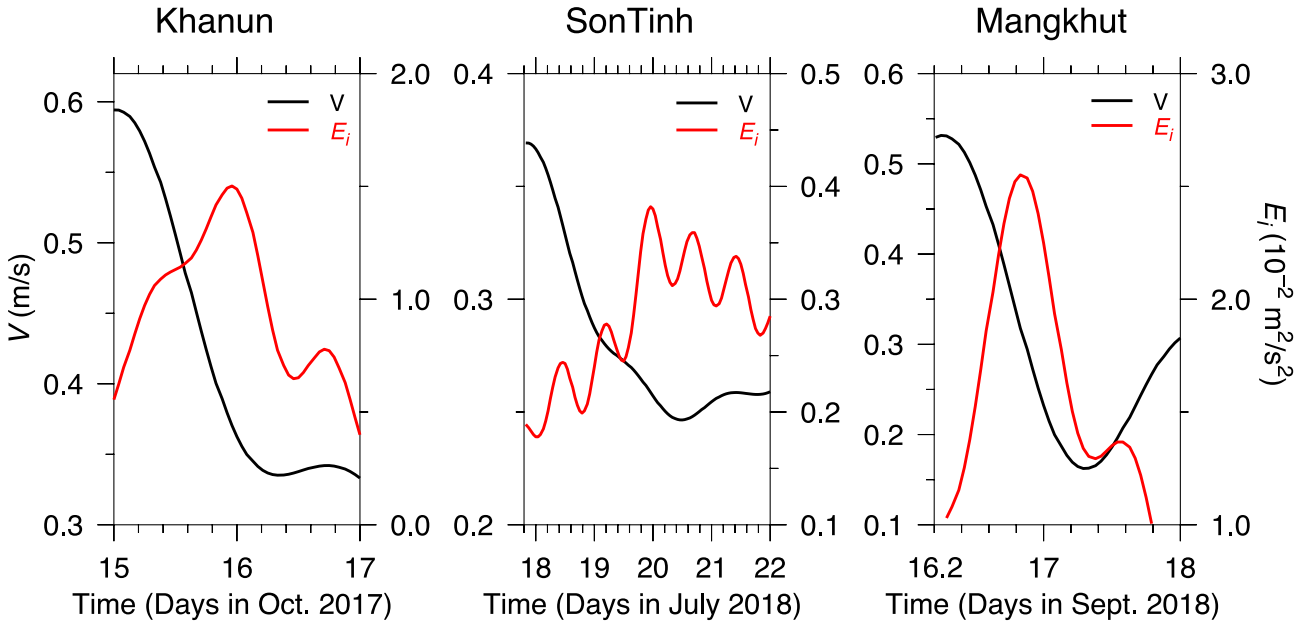

Figure 15. Changes of the along-shelf low-frequency current (V) and inertial energy (E_I) at site M2 estimated by Equation 5 during the crossing period of Khanun, SonTihn, and Mangkhut.

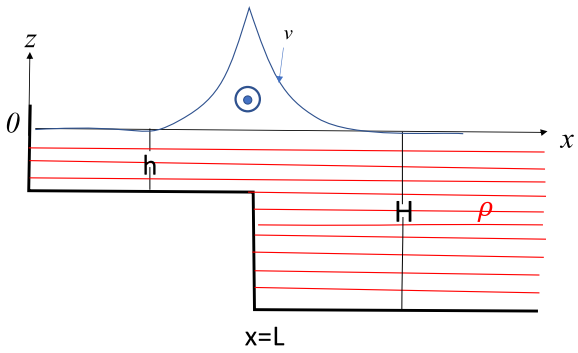

Figure 16. Illustration of an idealized step-topographic shelf. The red line is an indicator of the contours of the water density. *h* and *H* are the water depths in shallow and deep regions, respectively. The curve on the top indicates the distribution of the along-shelf flow with a maximum at the edge of the shallow shelf and decay exponentially onto and off the step-slope. A symbol with a dot in a circle presents a velocity direction. Facing the direction the water moves toward, the shallow water is on the right.

Under a stratified condition, the NIOs could behave like near-inertial interval waves with the Wentzel-Kramers-Brillouin (WKB)-approximate normalized horizontal velocity defined as

$$\bar{V}_n(z) = \bar{V}(z) \times \left(\bar{N} / N\right)^{1/2} \tag{8}$$

where $\overline{V_n}(z)$ is normalized velocity; $\bar{V}(z)$ is original velocity; and $\bar{N}$ is the mean buoyancy frequency (Leaman & Sanford, 1975). In our case, the NIOs occurred in both the upper mixed and lower stratified layers. We cannot directly apply Equation 8 to all TC's case, especially for Khanun, during which the water was vertically mixed in the upper layer and at the shallow mooring sites. We calculated the normalized near-inertial velocity using Equation 8 for SonTinh and compared it with the band-passed filtered velocity. The vertical and cross-shelf distributions of NIOs remain unchanged for both the cases (Figure 19), suggesting that the band-passed results are robust for our studies.

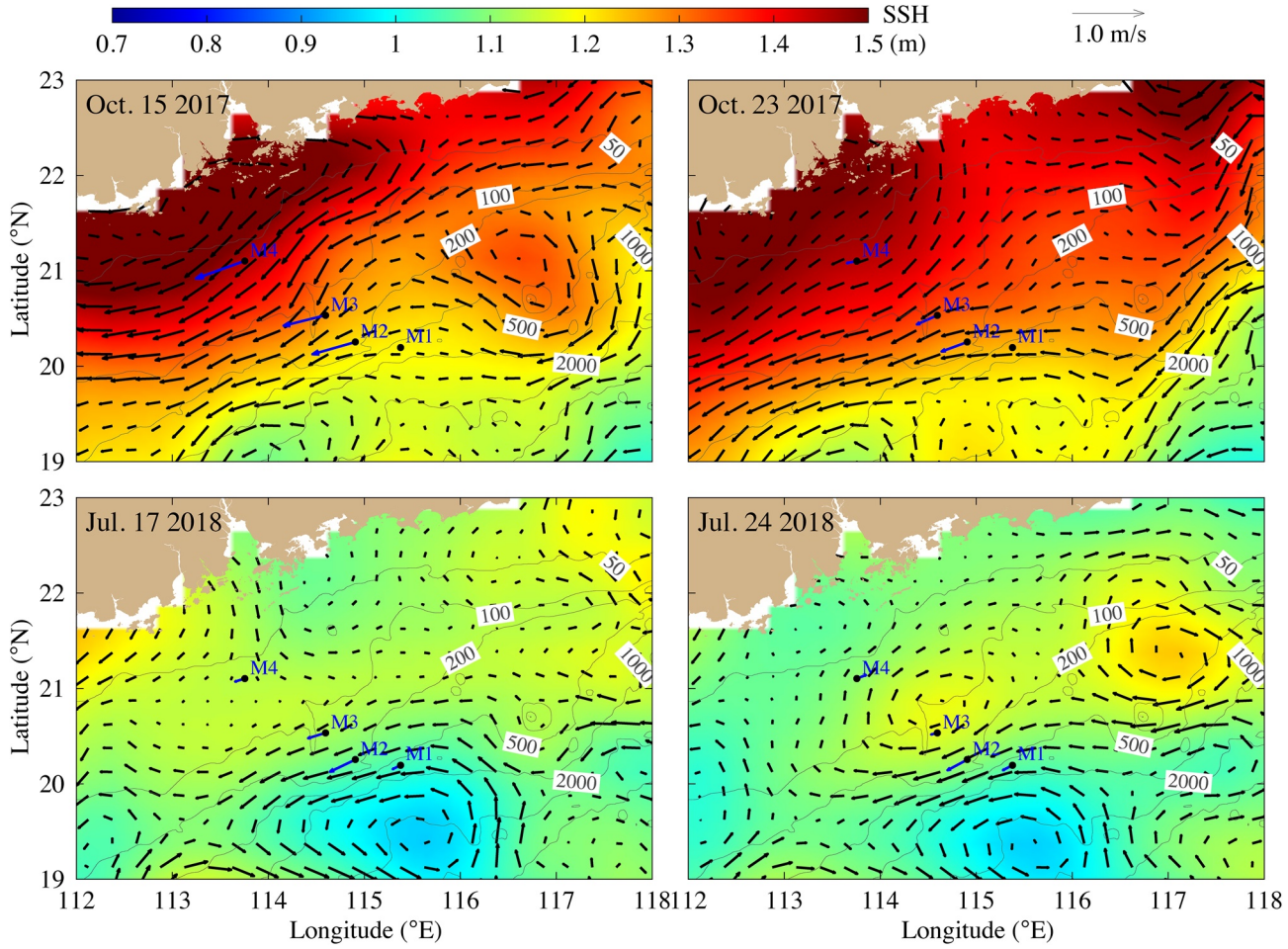

Figure 17. Distribution of the SSH (m) and SSH-derived geostrophic current vectors over the northern shelf of the SCS on October 15 and 23, 2017 (upper panels) and July 17 and 24, 2018 (lower panels). The blue vectors overlapped on each figure are the daily and vertically averaged current vectors observed at the mooring sites. M1–M4 are the names of the moorings. The light gray curves are the water depth contours with a unit of meters. SSH, sea surface height; SCS, South China Sea.

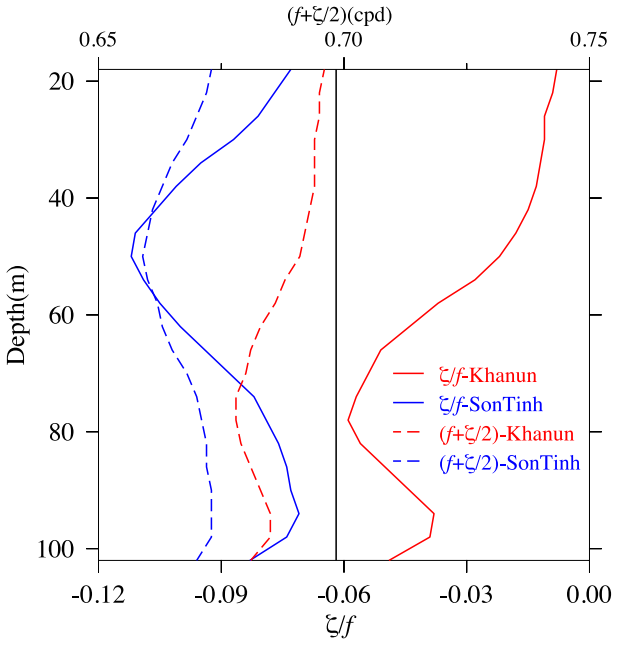

Figure 18. Vertical profiles of the mean vorticity and effective Coriolis frequency calculated based on the observed long-shelf velocities at the sites M2 and M3 for Khanun and SonTinh, respectively. The mean vorticity is determined by averaging the hourly vorticity profiles over October 15–27, 2017 for Khanun and July 18–31, 2018 for SonTinh. The mean effective Coriolis frequency is calculated using the mean vorticity.

5. Conclusions

We examined the storm-induced NIOs across the northern shelf of the SCS, a region vulnerable to TCs. An array of eight moored current meters and two meteorological buoys were deployed within major pathways of TCs across the northern shelf of the SCS. This array captured three TCs; Khanun, SonTinh, and Mangkhut in October 2017, July, and September 2018, respectively. These three TCs excited strong NIOs over the northern shelf of the SCS, which were slope-intensified over the slope regardless of the trajectories and intensities of TCs. In the vertically well-mixed area, the NIOs were relatively uniform throughout the water column with small amplitude and phase changes. In the stratified region, they were characterized by a two-layer structure, with strong oscillations in the upper mixed and lower stratified layers. The oscillation phase changed rapidly through thermoclines, with a vertical distribution, unlike the first baroclinic mode.

The tidal current energy also varies with season, especially for diurnal tides that were stronger in spring through early fall and weaker in late fall through winter. The observations do not show a significant tidal and near-inertial current nonlinear interaction. The harmonic waves detected from velocity measurements are likely due to the Doppler shift-induced "fine-structure contamination" pointed out by Alford (2001b).

During summer through fall, the slope of the northern shelf of the SCS is predominated by a southwestward low-frequency subtidal current. This flow was significantly intensified during TCs' traversing, which produced a negative vorticity field when the NIOs were excited. The negative vorticity was considerably larger during the SonTinh crossing period than during the Khanun crossing period, causing a frequency-shifting of NIOs in the range of 3.6%–5.6% for SonTinh and 0.4%–2.9% for Khanun. Since the effective Coriolis frequency is still significantly lower than the diurnal tidal frequency in this tropical region, the band-passed filter is robust to separate the NIOs and the diurnal tidal energies.

The slope-intensified feature of NIOs is likely due to the energy accumulation resulted from topographic inertial waves, negative vorticity-trapping, and the adjustment of low-frequency flow to the pre-storm condition. The sharp change of the bottom slope can lead to a maximum velocity at the shelf break at which volume transports in the shallow and deep regions must be equal. Since the largest negative vorticity occurred at the shelf break, the slope-intensified feature of NIOs could result from the energy-trapping by the negative vorticity field detected from a near-inertial wave model by Kunze (1985). The vorticity-trapping theory can explain why the intensity of NIOs was more vigorous at the shelf break during the SonTinh crossing period than during the Khanun crossing period, even though the wind intensity was much weaker in the SonTinh case. Our observations show that the NIOs were excited by storm-induced strong winds during the intensification period of subtidal currents, but the strongest NOIs occurred during an adjustment period of the low-frequency flow to a pre-storm equilibrium state. This finding suggests a significant energy transfer from the low-frequency flow to the inertial motion. All three mechanisms are related to the sloping topography change and the existence of the low frequency, along-shelf subtidal flow over the slope.

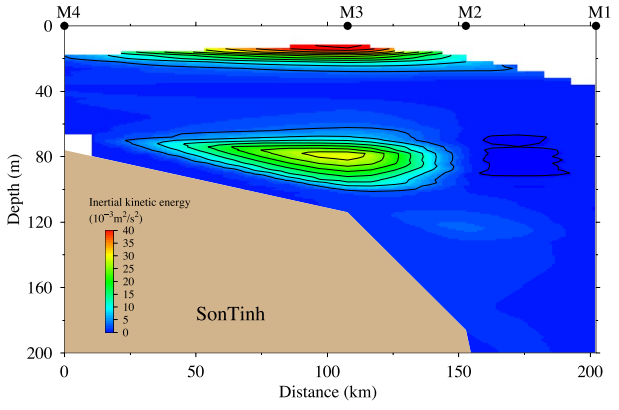

Figure 19. Cross-shelf distributions of the near-inertial oscillation energy calculated using the WKB-approximate normalized near-inertial velocity averaged over July 18–29, 2018 for SonTinh.

Data Availability Statement

All observational and model data used in this study can be downloaded at the link: http://fvcom.smast.umassd.edu/Data/FVCOM/NECOFS/Archive/Data_Li_etal_2020/

Acknowledgments
The authors want to thank many individuals in the South China Sea Survey and Technology Center who deployed, maintained, and recovered the moorings. This work was supported by the National Key Research and Development Programs of China with grant numbers 2018YFC-1406201; 2016YFA-0602700; 2018YFC-1506903; 2018YFC-1406205, and the Administrator Foundation of South China Sea Bureau of Ministry of Natural Resources (No.180106). They thank two reviewers for their constructive comments and suggestions that help improve the quality of our paper.

References

Alford, M. H. (2001a). Internal swell generation: The spatial distribution of energy flux from the wind to mixed layer near-inertial motions. *Journal of Physical Oceanography*, *31*, 2359–2368.

Alford, M. H. (2001b). Fine-structure contamination: Observations and a model of simple two-wave case. *Journal of Physical Oceanography*, *31*, 2645–2649.

Alford, M. H., MacKinnon, J. A., Simmons, H. L., & Nash, J. D. (2016). Near-inertial internal gravity waves in the ocean. *Annual Review of Marine Science*, *8*, 95–123. https://doi.org/10.1146/annurev-marine-010814-015746

Beardsley, R. C., Limeburner, R., & Rosenfeld, L. (1985). *Introduction: CODE-2 moored array and large scale data report* (85–35, 234). Woods Hole, MA: WHOI.

Brink, K. H. (1980). Propagation of barotropic continental shelf waves over irregular bottom topography. *Journal of Physical Oceanography*, *10*, 765–778.

Brink, K. H., & Chapman, D. C. (1985). *Programs for computing properties of coastal-trapped waves and wind-driven motions over the continental shelf and slope* (p. 98). Woods Hole, MA: Woods Hole Oceanographic Institution. https://doi.org/10.1575/1912/5368

Brink, K. H., Chapman, D. C., & Halliwell, G. R. (1987). A stochastic model for wind-driven currents over the continental shelf. *Journal of Geophysical Research*, *92*, 1783–1797.

Cao, A., Guo, Z., Song, J., Lv, X., He, H., & Fan, W. (2018). Near-inertial waves and their underlying mechanisms based on the south china sea internal wave experiment (2010–2011). *Journal of Geophysical Research: Oceans*, *123*, 5026–5040. https://doi.org/10.1029/2018JC013753

Chen, C., Reid, R. O., & Nowlin, W. D., Jr. (1996). Near-inertial oscillations over the Texas-Louisiana shelf. *Journal of Geophysical Research*, *101*, 3509–3524.

Chen, C., & Qin, Z. H. (1985). On geostrophic adjustment process of oceanic motions. *Scientia Sinica - Series B*, *28*, 1093–1100.

Chen, C., & Xie, L. (1997). A numerical study of wind-induced, near-inertial oscillations over the Texas-Louisiana shelf. *Journal of Geophysical Research*, *102*, 15583.

Chen, G., Xue, H., Wang, D., & Xie, Q. (2013). Observed near-inertial kinetic energy in the northwestern South China Sea. *Journal of Geophysical Research*, *118*, 4965–4977. https://doi.org/10.1002/jgrc.20371

Chen, S. L., Hu, J. Y., & Polton, J. A. (2015). Features of near-inertial motions observed on the northern South China Sea shelf during the passage of two typhoons. *Acta Oceanologica Sinica*, *34*, 38–43. https://doi.org/10.1007/s13131-015-0594-y

D'Asaro, E. A. (1985). The energy flux from the wind to near-inertial motions in the surface mixed layer. *Journal of Physical Oceanography*, *15*, 1043–1059.

Dong, W., Feng, Y., Chen, C., Wu, Z., Xu, D., Li, S., et al. (2020). Observational and modeling studies of oceanic responses and feedback to typhoons Hato and Mangkhut over the northern shelf of the south China Sea. *Progress in Oceanography*, *191*, 102507. https://doi.org/10.1016/j.pocean.2020.102507

Guan, S., Zhao, W., Huthnance, J., Tian, J., & Wang, J. (2014). Observed upper ocean response to typhoon Megi (2010) in the northern South China Sea. *Journal of Geophysical Research: Oceans*, *119*, 3134–3157. https://doi.org/10.1002/2013JC009661

Jaimes, B., & Shay, L. K. (2010). Near-inertial wave wake of Hurricanes Katrina and Rita over mesoscale oceanic eddies. *Journal of Physical Oceanography*, *40*(6), 1320–1337.

Kunze, E. (1985). Near-inertial wave propagation in geostrophic shear. *Journal of Physical Oceanography*, *15*, 544–565.

Kunze, E., & Sanford, T. B. (1984). Observations of near-inertial waves in a front. *Journal of Physical Oceanography*, *14*(3), 566–581.

Le Boyer, A. L., Alford, M. H., Pinkel, R., Hennon, T. D., Yang, Y. J., Ko, D., & Nash, J. (2020). Frequency shift of near-inertial waves in the South China Sea. *Journal of Physical Oceanography*, *50*, 1121–1135. https://doi.org/10.1175/JPO-D-19-0103.1

Leaman, K. D., & Sanford, T. B. (1975). Vertical energy propagation of inertial waves: A vector spectral analysis of velocity profiles. *Journal of Geophysical Research*, *80*, 1975–1978.

Li, R., Chen, C., Xia, H., Beardsley, R. C., Shi, M., Lai, Z., et al. (2014). Observed wintertime tidal and subtidal currents over the continental shelf in the northern South China Sea. *Journal of Geophysical Research: Oceans*, *119*, 5289–5310. https://doi.org/10.1002/2014JC009931

Liu, J., He, Y., Li, J., Cai, S., Wang, D., & Huang, Y. (2018). Cases study of nonlinear interaction between near-inertial waves induced by typhoon and diurnal tides near the Xisha Islands. *Journal of Geophysical Research: Oceans*, *123*, 2768–2784. https://doi.org/10.1029/2017JC013555

Mackinnon, J. A., & Gregg, M. C. (2005). Near-inertial waves on the New England Shelf: The role of evolving stratification, turbulent dissipation, and bottom drag. *Journal of Physical Oceanography*, *35*, 2408–2424. https://doi.org/10.1175/JPO2822.1

Pawlowicz, R., Beardsley, B., & Lentz, S. (2002). Classical tidal harmonic analysis including error estimates in MATLAB using T-TIDE. *Computers & Geosciences*, *28*(8), 929–937. https://doi.org/10.1016/S0098-3004(02)00013-4

Pollard, R. T. (1970). On the generation by winds of inertial waves in the ocean. *Deep-Sea Research*, *17*, 795–812.

Qi, H., Roland, A. D. S., & Clayton, A. P. (1995). The structure of near-inertial waves during ocean storms. *Journal of Physical Oceanography*, *11*, 2853–2871.

Sanford, T. B., Price, J. F., & Girton, J. B. (2011). Upper-Ocean response to Hurricane Frances (2004) observed by profiling EM-APEX floats. *Journal of Physical Oceanography*, *41*, 1041–1056. https://doi.org/10.1175/2010JPO4313.1

Schlosser, T. L., Jones, N. L., Bluteau, C. E., Alford, M. H., Ivey, G. N., & Lucas, A. J. (2019). Generation and propagation of near-inertial waves in a baroclinic current on the Tasmanian shelf. *Journal of Physical Oceanography*, *49*, 2653–2667. https://doi.org/10.1175/JPO-D-18-0208.1

Shay, L. K., & Elsberry, R. L. (1987). Near-inertial ocean current response to Hurricane Frederic. *Journal of Physical Oceanography*, *17*, 1249–1269.

Shay, L. K., Elsberry, R. L., & Black, P. G. (1989). Vertical structure of the ocean current response to a hurricane. *Journal of Physical Oceanography*, *19*, 649–669.

Shearman, R. K. (2005). Observations of near-inertial current variability on the New England shelf. *Journal of Geophysical Research*, *110*, C02012. https://doi.org/10.1029/2004JC002341

Shu, Y., Pan, J., Wang, D., Chen, G., Sun, L., & Yao, J. (2016). Generation of near-inertial oscillations by summer monsoon onset over the south china sea in 1998 and 1999. *Deep Sea Research I: Oceanographic Research Papers*, *118*, 10–19. https://doi.org/10.1016/j.dsr.2016.10.008

Sun, L., Zheng, Q., Tang, T., Chuang, W., Li, L., Hu, J., & Wang, D. (2012). Upper ocean near-inertial response to 1998 Typhoon Faith in the South China Sea. *Acta Oceanologica Sinica*, *31*, 25–32. https://doi.org/10.1007/s13131-012-0189-9

Sun, L., Zheng, Q., Wang, D., Hu, J., Tai, C., & Sun, Z. (2011). A case study of near-inertial oscillation in the South China Sea using mooring observations and satellite altimeter data. *Journal of Oceanography*, *67*, 677–687. https://doi.org/10.1007/s10872-011-0081-9

Sun, Z., Hu, J., Zheng, Q., & Li, C. (2011). Strong near-inertial oscillations in geostrophic shear in the northern South China Sea. *Journal of Oceanography*, *67*, 377–384. https://doi.org/10.1007/s10872-011-0038-z

Sun, Z. Y., Hu, J. Y., Zhen, Q. A., & Gan, J. P. (2015). Comparison of typhoon-induced near-inertial oscillations in shear flow in the northern South China Sea. *Acta Oceanologica Sinica*, *34*, 38–45. https://doi.org/10.1007/s13131-015-0746-0

Wang, G., Su, J., Ding, Y., & Chen, D. (2007). Tropical cyclone genesis over the South China Sea. *Journal of Marine Systems*, *68*, 318–326. https://doi.org/10.1016/j.jmarsys.2006.12.002

Yang, B., Hou, Y., Hu, P., Liu, Z., & Liu, Y. (2015). Shallow ocean response to tropical cyclones observed on the continental shelf of the northwestern South China Sea. *Journal of Geophysical Research*, *120*, 3817–3836. https://doi.org/10.1002/2015JC010783